DRAFT VERSION MARCH 16, 2018
Typeset using LaTeX **twocolumn** style in AASTeX61

VELOCITY FLUCTUATIONS IN THE MILKY WAY USING RED CLUMP GIANTS

SHOURYA KHANNA,[1,2] SANJIB SHARMA,[1,2] JOSS BLAND-HAWTHORN,[1,2,3] AND GALAH COLLABORATION[4]

[1] *Sydney Institute for Astronomy, School of Physics, A28, The University of Sydney, NSW, 2006, Australia*
[2] *Centre of Excellence for Astrophysics in Three Dimensions (ASTRO-3D), Australia*
[3] *Miller Professor, Miller Institute, UC Berkeley, Berkeley CA 94720*
[4] *GALAH*

ABSTRACT

Context: If the Galaxy is axisymmetric and in dynamical equilibrium, we expect negligible fluctuations in the residual line-of-sight velocity field. However, non-axisymmetric structures like a bar, spiral arms and merger events can generate velocity fluctuations. Recent results using the *APOGEE* survey claim significant fluctuations in velocity for stars in the mid plane ($|z|$ <0.25 kpc) out to 5 kpc and suggest that the dynamical influence of the Milky Way's bar extends out to the Solar neighborhood (Bovy et al. 2015). Their measured power spectrum has a characteristic amplitude of 11 km s^{-1} on a physical scale of ≈2.5 kpc. The existence of large-scale streaming motions on these scales has important implications for determining the Sun's motion about the Galactic Centre.
Aims: Using red clump stars from *GALAH* (Galactic Archaeology with HERMES) and *APOGEE* surveys, we map the line-of-sight velocity field around the Sun out to distances of 5 kpc and up to 1.25 kpc from the Galactic Plane.
Methods: By subtracting a smooth axisymmetric model for the velocity field, we study the residual velocity fluctuations and compare our findings with synthetic survey generated by *Galaxia* based on an axisymmetric, steady state model.
Results: We find negligible large-scale fluctuations away from the plane. In the mid-plane, we reproduce the *APOGEE* power spectrum but with 20% smaller amplitude (9.1 km s^{-1}) after taking into account systematic effects (e.g. window function). The amplitude power is further reduced to 6.9 km s^{-1} if a flexible axisymmetric model is used. Additionally, our mock simulations show that, in the plane, the distances are underestimated for high mass red-clump stars and this can lead to spurious power with amplitude of about 4.7 km s^{-1}. Taking this into account, we estimate the amplitude due to real fluctuations to be less than 5.1 km s^{-1}, about a factor of two below what is claimed by *APOGEE*.

Keywords: Galaxy: kinematics and dynamics – Stars: distances – Stars: fundamental parameters

Corresponding author: Shourya Khanna
skha2680@uni.sydney.edu.au

1. INTRODUCTION

The Milky Way is a late-type large disk galaxy. While the Galaxy has had a quiescent accretion history and has not had a major merger for the past 10 Gyr (Stewart et al. (2008), Bland-Hawthorn & Gerhard (2016)) it is orbited by nearby dwarf galaxies, some of which can cross the disk and perturb it. Some orbiting galaxies leave remnants such as the Sagittarius stream (Majewski et al. 2003). In addition, the Milky Way also hosts a central bar extending out to 5 kpc (Wegg et al. 2015), the dynamical effect of which can also be seen in the Solar-neighborhood as structures in velocity space, prominent examples include the Hercules stream (Dehnen (1998), Bovy (2010), Hunt et al. (2018) etc). And while it would seem natural to assume kinematic non-axisymmetry at small radii it is worth investigating whether the dynamical effects of the bar extend out to large radii such as around the Solar-neighbourhood. Studying the velocity substructure in the Milky Way thus holds clues to large scale evolutionary processes in the Galaxy.

Over the last two decades local surveys such as the Geneva-Copenhagen survey (*GCS*, Nordström et al. (2004)) and *RAVE* (Williams et al. 2013) have mapped the Solar-neighbourhood extensively and shown evidence of velocity gradients in the disk. With the advent of large-scale surveys it is now possible to venture out of the Solar-neighbourhood. For example, with *APOGEE*, Bovy et al. (2015) have mapped the disk in the mid-plane ($|z| < 0.25$ kpc) out to 15 kpc while with other ongoing surveys such as *GALAH* (Martell et al. 2017) and *LAMOST* (Zhao et al. 2012), we can now study the region away from the mid-plane and attempt to visualise kinematics in 3D.

The limitations of small scale surveys can be understood in the context of the local standard of rest (LSR) which is generally defined based on results from the *GCS* survey to be $(U,V,W)_\odot = (11.1, 12.24, 7.25)$ km s^{-1} (Schönrich et al. 2010). Using red-clump stars, Bovy et al. (2015) (hereafter B15) find streaming motions of 11 km s^{-1} on scales of 2.5 kpc and attribute this to the LSR moving with respect to the Galaxy on a non-axisymmetric orbit. This has important consequences for the value of $V_\odot$, the Sun's motion relative to the circular velocity ($V_{\rm circ}$) and would imply that the Solar-neighbourhood is moving ahead of the LSR. Although, the proper motion of Sgr A* is well constrained (Reid & Brunthaler 2004), there is still uncertainty on the distance of the Sun from the Galactic center ($R_\odot$). It is thus important to have multiple methods to constrain the Solar motion about the Galactic center. Robin et al. (2017) take this forward by making use of highly accurate proper motions from *GAIA* data release 1 (Gaia Collaboration et al. 2016) and *RAVE*-DR4 to model the asymmetric drift and leave the Solar motion as a free parameter. They propose a new much lower value for $V_\odot$ of 0.94 km s^{-1} but again their analysis is only restricted to the Solar vicinity.

Using a purely astrometric sample from GAIA-TGAS, Antoja et al. (2017) also use only proper motions to detect velocity asymmetries of about 10 km s^{-1} for positive and negative Galactic longitude. The asymmetry seems directed away from the Solar-neighbourhood and towards the outer disk. Similarly using SDSS-DR12 white dwarf kinematics, Anguiano et al. (2017) find $\partial V_R/\partial R = -3 \pm 5$ km s^{-1} and asymmetry in $< V_z >$ between the population above and below the plane of the Galaxy.

Given the compelling evidence of non-equilibrium kinematics shown by a diverse stellar population, it seems reasonable to perform a large scale 3D analysis of the Milky Way. In this paper we will look at the line-of-sight kinematics of red-clump (RC) stars selected from the *GALAH* and *APOGEE* spectroscopic surveys. In general, observed data has non-trivial selection function, and in some cases leaves a strong signature on the data. Not taking this into account can lead to spurious fluctuations. Hence it is imperative to check and compare the conclusion making use of a synthetic catalog of stars. To this end we make use of axisymmetric galaxy models using the *Galaxia*[1] code (Sharma et al. 2011).

Throughout the paper we adopt a right handed coordinate frame in which the Sun is at $R_\odot$=8.0 kpc from the Galactic center and has Galactocentric coordinates ($X_{\rm gc}$,$Y_{\rm gc}$,$Z_{\rm gc}$) = (-8.0,0,0). For transformation between heliocentric and Galactocentric frames we require the the Sun's radial and vertical motion with respect to the LSR $(U,W)_\odot$, and the the total azimuthal velocity about the Galactic center $V_\phi(R_\odot) = V_{circ}(R_\odot) + V_\odot$. Following Schönrich et al. (2010), we adopt $(U,W)_\odot = (11.1, 7.25)$ km s^{-1}, while for the azimuthal component we use the constraint set by the proper motion of Sgr A* on $\Omega_\odot$, the Sun's angular velocity around the Galactic center, where $\Omega_\odot = V_\phi(R_\odot)/R_\odot \approx 30.24$ km s^{-1}kpc^{-1} (Reid & Brunthaler 2004) .

The outline of the paper is as follows: In Section 2.1 we briefly describe our red-clump selection scheme, which includes using *Galaxia* to calibrate de-reddened colors against spectroscopic parameters in order to select a pure red-clump sample. This is used to derive distances in Section 2.2. Then in Section 3.1 we briefly discuss the observed and simulated datasets used in the paper. Our kinematic model and methods are described in Section 3.3. In Section 4.1 we test our model on a *Galaxia* all-sky sample and identify high mass

[1] *Galaxia* is a stellar population synthesis code based on the Besancon Galactic model by Robin et al. (2003). *Galaxia* uses its own 3D extinction scheme to specify the dust distribution and the isochrones to predict the stellar properties are from the Padova database (Marigo et al. (2008); Bertelli et al. (1994)). Full documentation is available at http://galaxia.sourceforge.net/Galaxia3pub.html

red-clump population as a contaminant. Next, in Section 4.2 we analyse observed data in the midplane and compare with the *APOGEE* result of B15. Then in Section 4.3 we extend the analysis to the offplane region and compare our results with selection function matched *Galaxia* realizations before discussing our findings in Section 5.

2. SELECTING PURE RED-CLUMP SAMPLE TO ESTIMATE DISTANCES

2.1. *Red-clump calibration and selection*

The Red clump (RC) is a clustering of red giants that have gone through helium flash and now are quietly fusing helium in the convective core. These stars on the Helium-burning branch of the Hertzsprung-Russell diagram (HRD), have long been considered 'standard candles' for stellar distances as they have a very similar core mass and luminosity (Cannon 1970). While many studies use the RC, there is considerable variation in literature over calibration for the absolute magnitude of these stars. Moreover, some passbands are more affected than others by metallicity variations within the RC population, although the K_s (hereafter K) band seems most reliable (Salaris & Girardi 2002). Studies using parallaxes from Hipparcos have shown that the average absolute magnitude M_{Ks} can range from -1.65 to -1.50 (Girardi 2016) and there is ongoing effort to revise this using *GAIA* (Hawkins et al. 2017). Given this variation, we won't assume single M_{Ks} value to estimate distances but will instead derive an empirical relation between K band absolute magnitude and metallicity [Fe/H]. In order to do this, however, we will first need to select a reliable sample of red-clump stars.

Our selection function is based in terms of de-reddened colors C_{JK} =$(J-K)_0$ and the spectroscopic parameters: surface gravity $\log g$, metallicity [Fe/H] and effective temperature $T_{\rm eff}$ as described in Bovy et al. (2014). In the *APOGEE* red-clump catalog (Bovy et al. 2014) the photometry is corrected for extinction using the Rayleigh Jeans Color Excess method (RJCE; Majewski et al. 2011)) which requires photometry in 2MASS and [4.5μ] bands. However, it is difficult to get de-reddened colors accurately just from photometry. So to overcome this, we use pure red-clump stars from *Galaxia* to derive empirical relations expressing C_{JK} in terms of [Fe/H] and $T_{\rm eff}$. This allows us to derive de-reddened colors from spectroscopic parameters, which we can then use to select the red-clump samples for any given spectroscopic sample. In particular, the *Galaxia* red-clump sample is also used to obtain the aforementioned M_{Ks}-[Fe/H] curve (see Table 5), which is used to estimate distances. The procedure above is described in full detail in Appendix A.

We now check the accuracy of our selection function in recovering the red clump stars. For this we compute precision (fraction of selected stars that are red-clumps) and recall (fraction of red clump stars that are selected), which are two commonly used measures of accuracy in the field of information retrieval. We find that 97.6% of our selected stars are red-clumps. Since our selection is based on spectroscopic parameters that have uncertainties associated with them, we also explored the effects of adding Gaussian errors of $(\sigma_{\log T_{\rm eff}}, \sigma_{\rm [Fe/H]}, \sigma_{\log g}) = (0.011, 0.05, 0.1)$ dex. For $T_{\rm eff} = 4700$, typical temperature of a red-clump star, the uncertainty in temperature is 120 K. In spite of the uncertainties, the precision of the selected stars was found to be 83% (see Table 1 for summary), however, the recall dropped to 69%. If the uncertainty on temperature is reduced by a factor of two, the precision increases to 91% and recall to 85%, suggesting that it is important get precise and accurate temperatures.

Table 1. Accuracy of the red-clump selection function as predicted by all-sky $J < 15$ mock samples from *Galaxia*. Shown are results for cases with: 1) no uncertainty on spectroscopic parameters; 2) with uncertainty typically expected from high resolution spectra, e.g., *APOGEE* (Holtzman et al. 2015) and 3) same as 2) but with smaller $\sigma_{\log T_{\rm eff}}$ which should be achievable with good quality spectra.

	$\sigma_{\log T_{\rm eff}}$ (%)	$\sigma_{\rm [Fe/H]}$ (%)	$\sigma_{\log g}$ dex	Recall[a] dex	Precision[b] dex	$\sigma_{\rm dmod}$[c] mag
1	0.0	0.0	0.0	1.0	0.976	0.10 (0.09)
2	0.011	0.05	0.1	0.692	0.831	0.16 (0.12)
3	0.0055	0.05	0.1	0.846	0.914	0.12 (0.11)

[a]We define red-clumps as those stars that satisfy equations (A1-A4). So, recall refers to fraction of total number of red-clump stars that are selected.
[b]Here precision refers to fraction of selected stars that have initial stellar mass $> M_{\rm RGB,tip}$
[c]The quantity in brackets denotes $\sigma_{\rm dmod}$ for the actual red clump stars, which is not significantly affected by addition of spectroscopic uncertainties.

2.2. *Distances*

We now proceed to estimate distances for our red-clump sample. The distance modulus for a given passband λ corrected for extinction is given by

$$d_{\rm mod} = m_\lambda - M_\lambda - A_\lambda, \tag{1}$$

with apparent magnitude m_λ, absolute magnitude M_λ and extinction A_λ. For the K band, M_λ is derived using our M_K-[Fe/H] relation (Table 5), while for the extinction we make use of the derived intrinsic colors $C_{JK}([{\rm Fe/H}], T_{\rm eff})$. (see equation A8) i.e.,

$$(J-K) - C_{JK} = (A_J - A_K), \tag{2}$$

and this can be related to the reddening E(B-V) using $f_\lambda = A_\lambda)/E(B-V)$ as

$$(A_J - A_K) = (f_J - f_K) E(B-V). \tag{3}$$

After rearranging we get the general relation

$$A_\lambda = f_\lambda \times \frac{(J-K)-C_{JK}}{f_J - f_K}, \quad (4)$$

with f_λ as in Schlegel et al. (1998) (see Table 4).

To illustrate the accuracy achieved in estimating distances for the *Galaxia* sample, we show the residuals in $d_{\rm mod}$ with respect to the true distance modulus in Figure 1. The residuals lie close to zero, with a typical distance uncertainty of 4%. There is also no significant bias as a function of metallicity [Fe/H]. If uncertainty in spectroscopic parameters are taken into account the dispersion in estimated distance modulus $\sigma_{\rm dmod}$ increases and this is shown in Table 1 for some typical cases. The main reason for the increase in $\sigma_{\rm dmod}$ is the contamination from stars that are not red clumps, e.g., RGB stars, which can be understood from the quoted precisions in the table. The quantity in brackets denotes $\sigma_{\rm dmod}$ for the actual red clump stars, which is not significantly affected by addition of spectroscopic uncertainties.

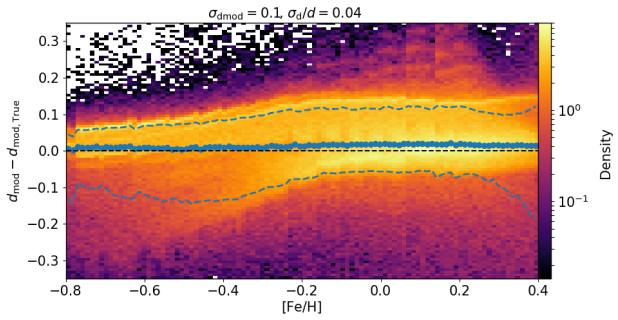

Figure 1. Distance accuracy using red-clump calibration on *Galaxia*: The residuals in the distance modulus are concentrated close to zero (black dotted line) and there is no significant bias with metallicity. The blue dotted lines indicate the 1σ bounds, with the overall distance error being 4 %.

3. DATA AND METHODS

3.1. *Datasets*

In this paper we make use of data from the *APOGEE* and *GALAH* surveys from which red-clump stars are selected using the selection scheme described in Appendix A unless otherwise specified. Following is a brief overview of the datasets used for our analysis:

We downloaded the red-clump catalog of *APOGEE* DR12[2], in order to compare our results directly with Bovy et al. (2015). This dataset contains 19937 stars and will be referred to as *ADR12RC*. Similarly we also obtained the latest *APOGEE* DR14[3] red-clump catalog. This contains 29502

[2] APOGEE DR12-RC fits files
[3] APOGEE DR14-RC fits files

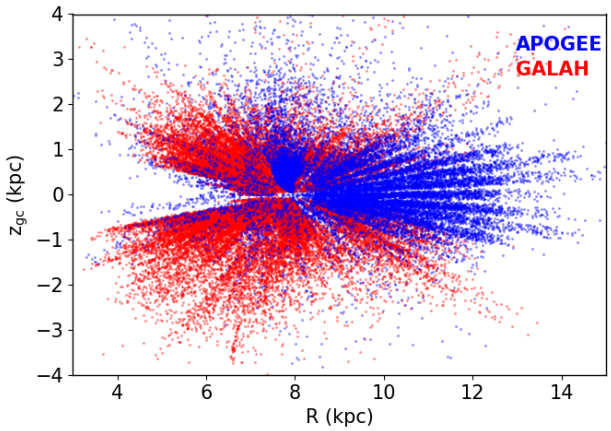

Figure 2. Distribution of the combined red-clump dataset GADR14RC in Galactocentric $R-z$ plane. While the *APOGEE* coverage dominates in plane and towards the anti-center, *GALAH* surveys the off-plane region more extensively.

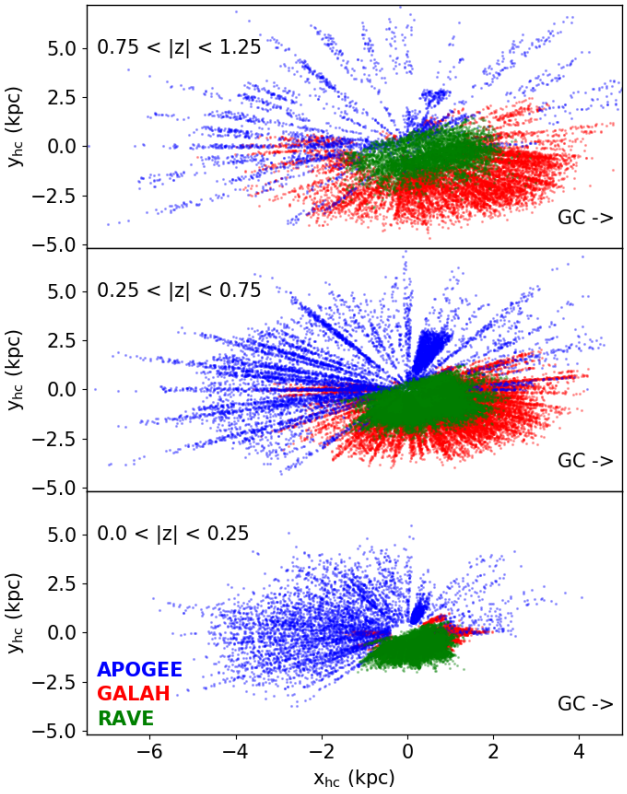

Figure 3. Distribution of GADR14RC in heliocentric (x,y) coordinates where the symmetrical regions above and below the plane have been merged together in z slices of 500 pc. *APOGEE* probes deep into the disk while *GALAH* provides good coverage moving away from the plane, and to illustrate this also shown is the coverage of RAVE DR5.

stars and will be referred to as *ADR14RC*. In both cases, while we do not apply our red-clump selection method, we do estimate the distances using the scheme in Section 2.2. Our distances were found to be in excellent agreement with those in *APOGEE* red-clump catalog. In our analysis the distances are used to compute velocity maps, and we found that there was no difference between the velocity maps computed using either of the distances. Where it appears the additional tag 'SF_Bovy' explicitly means that the dataset used has exact selection as in the *APOGEE* red-clump catalogs.

Next, from the internal release of *GALAH* data up to October 2017 we preselect stars in the magnitude range $9 < V < 14$. The data includes fields observed as part of the *K2-HERMES* (Wittenmyer et al. 2018) and *TESS-HERMES* (Sharma et al. 2018) programs but not the fields observed as part of the pilot[4] survey. Also, data without a proper selection function (field id <-1) was excluded from the analysis. The spectroscopic parameters are from the same pipeline that was used in Sharma et al. (2018) and further details of spectroscopic analysis can be found there and in Duong et al. (2018). Details on reduction and estimation of radial velocity are in Kos et al. (2017). From the full data we select red-clump stars using our scheme in Appendix A and obtain 29693 RC stars. This is merged with *ADR14RC* to form a combined observed dataset called *GADR14RC* and again where it appears, the additional tag 'SF_New' signifies that our selection method was employed. This combined set provides a more complete (x, y) spatial coverage as shown in Figure 2 and Figure 3, where only for comparison we show 44166 red-clump stars from *RAVE*-DR5 (Kunder et al. 2017) using our selection scheme. The combined dataset allows us to explore the region well beyond the Solar-neighbourhood.

Finally, we use *Galaxia* to simulate the selection functions of *APOGEE*[5] (Zasowski et al. 2013) and *GALAH* (Martell et al. 2017) and generate a combined red-clump dataset using our selection schemes for direct comparison with *GADR14RC*. Finally, for Section 4.1 we also generate an all-sky mock red-clump catalog to test our kinematical models. All *Galaxia* samples were generated with the 'warp' option turned off in order to allow easier interpretation of our experiments.

3.2. *Proper motions*

In order to transform from the heliocentric to Galactocentric frame we require highly accurate proper motions. Gaia DR1 has provided high precision parallaxes for about 2 million objects and the DR2 (expected April 2018) will extend this to nearly a billion objects and will also provide proper motions. In the meantime the two extensively used proper motion catalogues PPMXL (Roeser et al. 2010) and UCAC4 (Zacharias et al. 2013) have been improved using Gaia DR1 positions (UCAC5, Zacharias et al. (2017); HSOY (**H**ot **S**tuff for **O**ne **Y**ear), Altmann et al. (2017)). Until Gaia DR2 these updated catalogues will provide proper motion with 1-5 mas/yr precision. For all our observed datasets, where available, we use the average of UCAC5 & HSOY values, and default (UCAC4) proper motions elsewhere. We have checked that this has no impact on our results. Moreover, our main analysis does not make use of proper motions.

3.3. *Kinematic model*

In this section we will describe the framework of our kinematical modelling. Our goal is to reproduce the observed line-of-sight velocity field ($V_{\rm los}$) using an axisymmetric Galactic model. In our scheme the Galactocentric velocity distribution, $V = (V_R, V_z, V_\phi)$, follows the triaxial *Gaussian* distribution

$$p(V|r,\tau) = \frac{1}{\sigma_R\sigma_\phi\sigma_z(2\pi^{3/2})}\exp\left\{\frac{V_R^2}{\sigma_R^2}+\frac{V_z^2}{\sigma_z^2}+\frac{(V_\phi-\overline{V}_\phi)^2}{\sigma_R^2}\right\}, \tag{5}$$

where we assume that $\overline{V}_{\rm R}$ and $\overline{V}_{\rm z}$ are negligible, while $\overline{V}_\phi$ can be expressed as

$$\overline{V}_\phi^2 = V_{\rm circ}^2(R,z)+\sigma_R^2\left(\frac{{\rm d}\ln\rho}{{\rm d}\ln{\rm R}}+\frac{{\rm d}\ln\sigma_{\rm R}^2}{{\rm d}\ln{\rm R}}+1-\frac{\sigma_\phi^2}{\sigma_R^2}+1-\frac{\sigma_z^2}{\sigma_R^2}\right), \tag{6}$$

in terms of the Galactocentric circular velocity $V_{\rm circ}$, and the asymmetric drift as given by Binney & Tremaine (2008) for the case[6] where the principle axis of the velocity ellipsoid is aligned with the spherical coordinate system (r, θ, ϕ) centered on the Galactic center. There is however, evidence to suggest that the ellipsoid is aligned with the cylindrical system (R, ϕ, z) (Binney et al. 2014), in which case $\overline{V_R V_z} = 0$ and this would remove the z dependence. Since the actual answer probably lies in between the two alignments, we instead define a parameter $c_{\rm ad}$ to take this into account.

$$\overline{V}_\phi^2 = V_{\rm circ}^2(R,z)+\sigma_R^2\left(-\frac{R}{R_{\rm d}}-\frac{2R}{R_\sigma}+\overbrace{1-\frac{\sigma_\phi^2}{\sigma_R^2}+1-\frac{\sigma_z^2}{\sigma_R^2}}^{c_{\rm ad}}\right). \tag{7}$$

Here we have assumed exponential density profiles for the Galactic disk ($\rho \propto e^{-R/R_d}$, Sharma & Bland-Hawthorn (2013)) and velocity dispersion ($\sigma \propto e^{\frac{R-R_\odot}{R_\sigma}}$). If $\sigma_{\phi,R,z} \propto \exp(-R/R_\sigma) f_{\rm AVR}(\tau)$, where $f_{\rm AVR}$ is the age velocity dispersion relation and τ the age, then $c_{\rm ad}$ is a constant. Using the above framework we can now describe the individual models employed:

[4] Data collected before March 2014 i.e., with cob id< 1403010000 is excluded, where cob id = date*10000 + run no.

[5] APOGEE DR14 fields

[6] $\overline{V_R V_z} = V_R^2 - V_z^2(z/R))$

Table 2. Correction for age-velocity relation.

$\overline{\lvert z\rvert}$	0.0	0.5	1.0	2.0
δ_{σ_0}	0.0	5.0	7.0	7.0

- *Bovy1*: The model used by B15 is derived in (Bovy et al. 2012) (B12 hereafter). Essentially they assume $\overline{V_R V_z} = 0$, exponential surface density profile, exponential velocity dispersion profile and a constant circular velocity and then use the distribution function from Dehnen (1999) to model the asymmetric drift. Sharma et al. (2014) fitted the B12 model to *RAVE* data and showed that the B12 model can be approximated by setting $c_{\rm ad} = 1 - 0.85^2 = 0.28$. In order to reproduce the results of B15 we adopt this value for $c_{\rm ad}$. Furthermore, in accordance with B15, we set the radial and dispersion scale lengths $R_d = 3$ kpc and $R_\sigma = \infty$ kpc respectively, assume a flat profile for the circular velocity $V_{\rm circ} = 220$ km s^{-1}, $V_{\rm circ} + V_\odot = 242.5$ km s^{-1} and $\sigma_R = 31.4$. We use *Bovy1* only for the mid-plane ($|z| < 0.25$ kpc) as was the case in B15.

- *Strom_z*: This is the model that best captures kinematics in *Galaxia*. For simulating the kinematics, instead of the default model in *Galaxia* we adopt the RAVE-GAU kinematic model from Sharma et al. (2014) (last column of Table 6), which gives $c_{\rm ad} = 0.77$. The disk and velocity dispersion scale lengths are $(R_d, R_\sigma) = (2.5, 13.7)$ kpc. For the thick disk we assume a mono-age population (11 Gyr old) and for simplicity we assume that the thick disc obeys the AVR of the thin disc. Lastly, in *Galaxia* we use $V_{\rm circ} + V_\odot = 226.84 + 12.1$ km s^{-1} and the circular velocity profile is from Sharma et al. (2011) and is not flat.

  Now we describe the model that we use to fit data obtained from *Galaxia*. In the observed data ages are not known, so we derive how σ_R changes with z and adopt the following form

$$\sigma_R(R,z) = (\sigma_0 + \delta_{\sigma_0}(z)) \exp(-R/R_\sigma). \tag{8}$$

  Here $\sigma_0 = 30.7$ km s^{-1}. The term δ_{σ_0} is a function of $|z|$ and is used to account for the fact that the age increases with height above the disk. The term is obtained by interpolation from Table 2.

- *globalRz*: The approach in B15 requires making assumptions about the circular velocity profile as well as the ratio of the radial to azimuthal velocity dispersions. Typically, $\sigma_{\rm R}$ in the disk lies around 20-40 km s^{-1}(Bovy et al. 2012), however proper modelling of the AVR requires a good handle on stellar ages. Moreover, $V_{\rm circ}$ itself has a non-trivial profile, as for example was found with kinematic analysis of *RAVE* where gradient in both radial ($\propto \alpha_R(R - R_\odot)$) and vertical directions ($\propto \alpha_z |z|^{-1.34}$) was reported (Sharma et al. 2014). Furthermore, if we compute $\overline{V}_\phi$ using proper motions, we see that the profiles are not flat in R (Figure 4).

  Given that some of the assumptions might not be correct, for our analysis we adopt a flexible model for $\overline{V}_\phi$, that is a 2^{nd} order polynomial in R and z, more specifically,

$$\overline{V}_\phi = \sum_{i=0}^{2}\sum_{j=0}^{2} a_{ij} (R - R_\odot)^i z^j, \tag{9}$$

  which can be transformed from Galactocentric to heliocentric coordinates to forward model the line-of-sight velocity $V_{\rm los,mod}$. This does not require assuming a value for $V_\odot$ or $V_{\rm circ}$ as we use the proper motion of Sgr A* as a constraint. In order to fit for the coefficients a_{ij} we assume that the observed $V_{\rm los}$ is a Gaussian $\mathcal{N}(.||{\rm mean}, {\rm dispersion})$ centered at $V_{\rm los,mod}$ with dispersion $\sigma_{\rm V} = 31.4$ km s^{-1} along R and ϕ. This can be summarized as,

$$p(V_{\rm los}|\alpha_{\rm i}, l_{\rm gc}, z_{\rm gc}, R) = \mathcal{N}(V_{\rm los}|V_{\rm los,mod}, \sigma_v), \tag{10}$$

  and we call this model *globalRz*. The *MCMC* fitting is carried out using the *bmcmc* package (Sharma 2017).

3.4. *Fourier analysis of velocity fluctuations*

Each dataset is divided into three slices in z (as in Figure 3), and further binned into (x, y) pixels of 0.75×0.75 kpc^2. For each bin, we calculate the residual $\Delta V_{\rm los} = V_{\rm los} - V_{\rm los,mod}$ and produce a 2D velocity fluctuation map. On this we then perform 2D-Fourier analysis following Bovy et al. (2015) to calculate the power spectrum of fluctuations,

$$P(k_{\rm x}, k_{\rm y}) = \frac{1}{NM} A_{kl} \Delta x \Delta y, \tag{11}$$

where,

$$A_{\rm kl} = \sum_{i=0}^{2N}\sum_{j=0}^{2M} a_{\rm ij} exp(-\pi I(ik/N + jl/M))), \tag{12}$$

with N,M the no.of (x, y) bins. $P(k_{\rm x}, k_{\rm y})$ is azimuthally averaged in bins of $k = \sqrt{(k_x^2 + k_y^2)}$ and we present this 1D power spectrum $P(k)$ as our final result. The noise for the power spectrum is calculated in the same manner except that for the input signal we use normally distributed data with zero mean and dispersion equal to the standard deviation of $\Delta V_{\rm los}$.

4. RESULTS

The observed data has complicated selection functions in terms of magnitude and spatial coverage. Therefore before

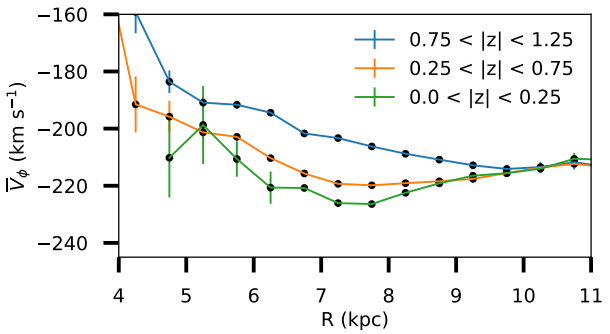

Figure 4. Mean Galactocentric rotation ($\overline{V}_\phi$) derived using proper motions for the combined dataset GADR14RC and shown for different z slices. The profiles look parabolic in nature with a steepening gradient as we move away from the plane.

we study the observed data, we will first consider a much simpler dataset using *Galaxia* that has uniform spatial coverage. This will allow us to test the method described in Section 3.3 and explore any selection function related biases.

4.1. *Galaxia all-sky sample: High mass red-clump stars*

Using *Galaxia* we generate an all-sky sample that has $H < 13.8$, the magnitude boundary of the *APOGEE* data set in the mid-plane, and select red-clumps using the scheme in Appendix A. We make three versions of this dataset, one with true distances ($d = d_{\rm True}$), one with with red-clump-derived distances ($d = d_{\rm RC}$) and one with red-clump-derived distances but only for stars with $d_{\rm RC}/d_{\rm True} > 0.8$. The last one being a control sample to check for systematic errors in distances. For each data set we fit the *globalRz* kinematic model to $V_{\rm los}$ data and derive the $\overline{V}_\phi$ profile and then construct the $\Delta V_{\rm los}$ map (Section 3.3). In Figure 5, we only show results for the mid-plane region with $|z| < 0.25$ kpc. The panels in first column compare the derived $\overline{V}_\phi$ profile with the actual $\overline{V}_\phi$ profile, computed directly using line-of-sight motion, proper motions and true distances. The $\overline{V}_\phi$ profile computed using red-clump distance is also shown alongside. The panels in second column show the map of velocity fluctuations $\Delta V_{\rm los}$, while their power spectrum is shown in panels of the third column. Finally, in the fourth column we show the map of distance residuals. The results for each case are summarized below.

- True distances $d = d_{\rm True}$: It is clear that for the true distances we are able to recover the profile by fitting *globalRz* model to $V_{\rm los}$. This is also reflected in the map of $\Delta V_{\rm los}$, where we obtain a smooth map with negligible residuals. Furthermore, the 1D power spectrum also has amplitude consistent with noise of about 2 km s^{-1}. This scenario is as would be expected of a perfectly axis-symmetric galaxy.
- RC distances $d = d_{\rm RC}$: The results are more interesting for the red-clump derived distances case. Here, the actual $\overline{V}_\phi$ profile (green line) is not reproduced accurately by the *globalRz* model (blue line) unlike the previous case. The model overestimates the profile beyond the Solar circle ($R_\odot$) and underestimates it towards the Galactic center. The $\overline{V}_\phi$ profile computed using proper motions also does not match the actual profile. The $\Delta V_{\rm los}$ residual map shows a peculiar dipole along the y axis for $x > 0$. This feature gives rise to a sharp peak in the power spectrum with amplitude of 11.4 km s^{-1}at a physical scale of $k^{-1} = 1.6$ kpc. Exactly at the location where we see high residuals in $V_{\rm los}$ we also see high residual in distances.
- RC distances but only for $d_{\rm RC}/d_{\rm True} > 0.8$: The results of this case are very similar to that for case where we use true distances.

For the first case with true distances the residuals in both $V_{\rm los}$ and distance are zero by definition. For the second case with RC distances, we see significant residuals. It is clear that the region corresponding to the high $\Delta V_{\rm los}$ residual also corresponds to high distance residual, i.e., distance errors. This suggests the cause of high residuals is systematic errors in distances. This is further confirmed by the results of the third case, where we restrict the analysis to stars with $d_{\rm RC}/d_{\rm True} > 0.8$ and find no residuals in $V_{\rm los}$ or distances.

For the second case, the distance residuals are negative which means that the distances are underestimated. This would have the effect of bringing stars closer to us than in reality, more importantly, their kinematics would be inappropriate for their inferred location. This is why we see a dipole in the $V_{\rm los}$ maps. Since the velocity field is incorrect, the best fit *globalRz* model fails to reproduce the actual $\overline{V}_\phi$ profile. Due to systematics in distances the velocity profile inferred using proper motion would also be wrong, and this is the reason for the mismatch of the orange line with the green line in Figure 5b. Again this is confirmed in Figure 5c, where we restrict stars to $d_{\rm RC}/d_{\rm True} > 0.8$ and there is no mismatch between any of the $\overline{V}_\phi$ profiles.

We now investigate the cause for systematic errors in distances of red-clump stars. We generate an all sky $H < 13.8$ sample with Galaxia, identify red-clump stars in it, and then study their properties. Figure 6a, shows the distribution of red-clump stars in the plane of $M_{\rm K_s}$ and stellar mass M. Typically, red-clump stars have $M_{\rm K_s} \approx -1.60$, however Figure 6a shows that there is a tail extending down to much brighter magnitudes. Stars with $d_{RC}/d_{\rm True} < 0.8$ that were responsible for strange features in residual velocity maps in Figure 5 correspond to $M_{\rm K_s} < -2$ and this is shown as the black dashed line in the panel. In the tail below the line, brightness is strongly correlated with stellar mass, which extends up to 4

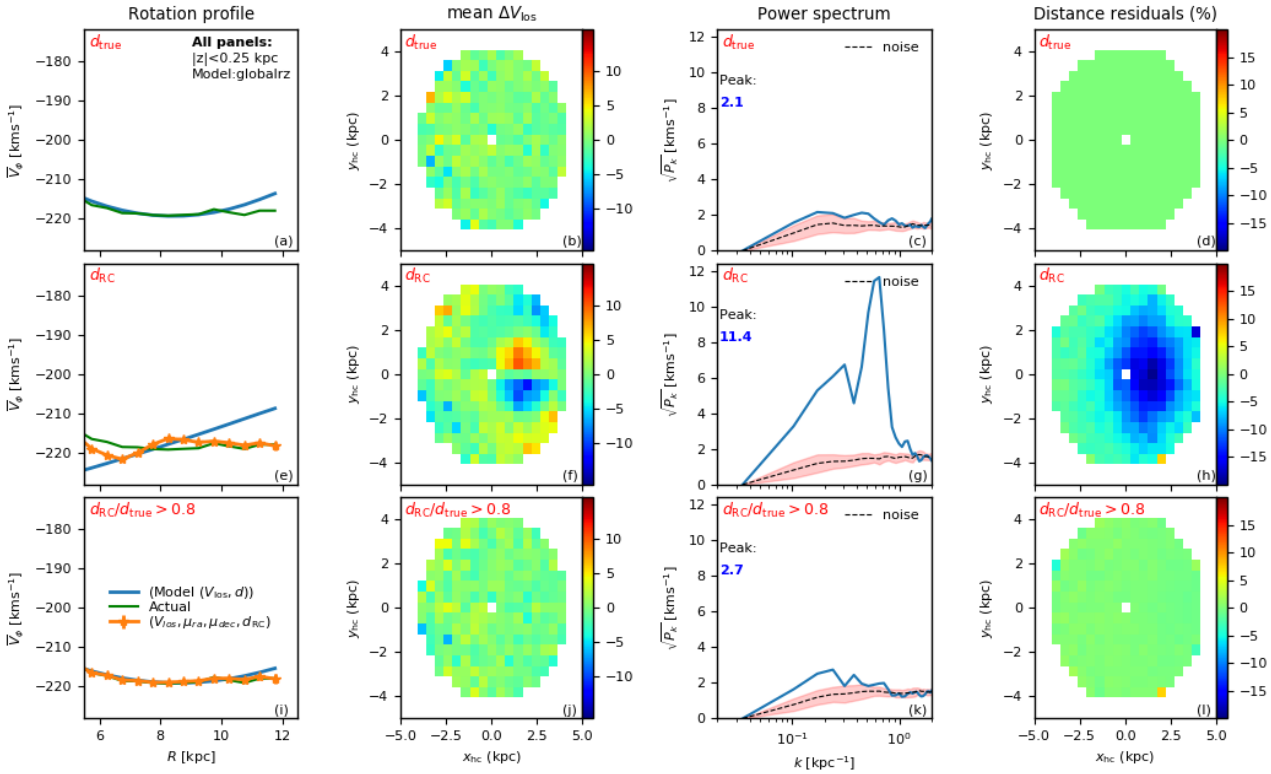

Figure 5. Kinematic modelling of *Galaxia* all-sky sample. Results with three different choices of distance are shown, true distances (Top panels), red-clump distances (Middle panels) and red-clump distances but with stars restricted to $d_{\rm RC}/d_{\rm True} > 0.8$ (Bottom panels). Each column shows a different aspect of the kinematics. (a,e,f): The $\overline{V}_\phi$ as function of R obtained by fitting the *globalRz* model to $V_{\rm los}$. The actual $\overline{V}_\phi$ profile and the profile obtained with proper motion and $d = d_{RC}$ is also plotted alongside. (b,f,j) The line-of-sight residual velocity map obtained after subtracting the best fit *globalRz* model. (c,g,k) Power spectrum of the residual velocity map. (d,h,l) Map of distance residuals computed with respect to $d_{\rm True}$.

$M_\odot$. We know that mass of a red giant star is anti-correlated with age (Sharma et al. 2016; Miglio et al. 2017), with massive stars being in general younger. So the cause for the systematic errors in the red-clump distances is the presence of young red-clump stars that have high mass and luminosity.

The anti-correlation of absolute magnitude with mass is easy to understand. Red clumps lie in a narrow range of $T_{\rm eff}$. Hence their luminosity L is proportional to R^2. Given that surface gravity $g = M/R^2$, we have

$$M_K \propto -2.5 \log L \propto -2.5(\log M - \log g) \quad (13)$$

$$M_K - 2.5 \log g \propto -2.5 \log M \quad (14)$$

For a given $\log g$, the magnitude decreases with mass and the expected trend is shown in Figure 6a. For red-clump stars $\log g$ is not constant, to take this into account in Figure 6b, we show stars in the $(M_K - 2.5 \log g, \text{Mass})$ space. The stars now perfectly follow the predicted relation of $-2.5 \log M$.

We now investigate as to where we expect to find such high mass stars and in which regions do we expect significant errors in distances. Figure 7a shows the map of distance residual in the (x, z) plane. We see that the distance residuals are high in the mid-plane of the Galaxy and towards the Galactic Center. In Figure 7b, we plot the fraction of red-clump stars that have $M_{\rm K_s} < -2$, i.e., very luminous. Close to the plane and towards the Galactic Center in certain areas the fraction is higher than 0.3. The regions of high distance residuals correspond to region with higher fraction of high-mass red-clump stars, this provides a causal link for the high distance residuals.

Why is the contamination from young-high-mass red-clump stars so prominent close to the plane and towards the Galactic Center? This is due to a combination of three different effects. Firstly, due to the age scale height relation in the Galaxy, younger stars have smaller scale height and are closer to the plane. Secondly, the surface density profile of stars in the Galaxy falls off exponentially with distance from the Galactic Center, which means there are more such stars towards the Galactic Center. Finally, along any given line-of-sight the volume of a cone around it increases as square of the distance. So more stars from far away with larger true distances are displaced to regions with smaller apparent distances.

We also studied the off plane slices and found no peculiar features in the residual velocity maps. This is expected as the

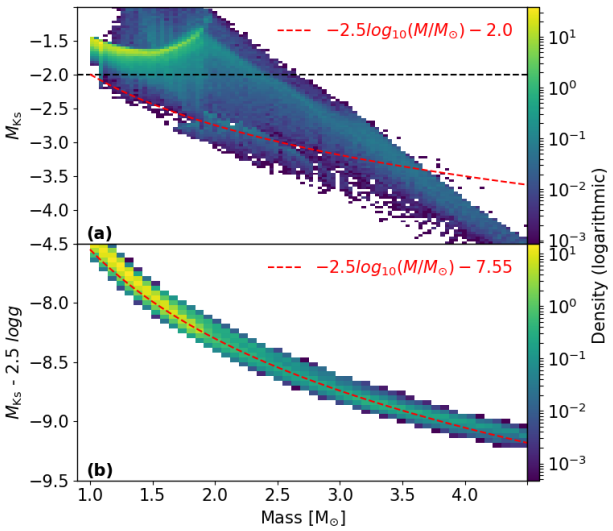

Figure 6. Mass distribution of red clump stars for a $H < 13.8$ sample simulated with *Galaxia*. Panel (a) shows the distribution of red clump stars in the (M_{K_s}, Mass) plane. It is clear that the luminous red clump stars also have higher mass. Stars above the black dashed roughly correspond to where $d_{\rm RC}/d_{\rm True} > 0.8$. Panel (b) shows the distribution of red clump stars in the ($M_{K_s} - 2.5\log g$, Mass) plane. The tight relation is because the red-clump stars lie in a narrow range of $T_{\rm eff}$. The red dotted line is $= -2.5\log {\rm M}$ in both the panels.

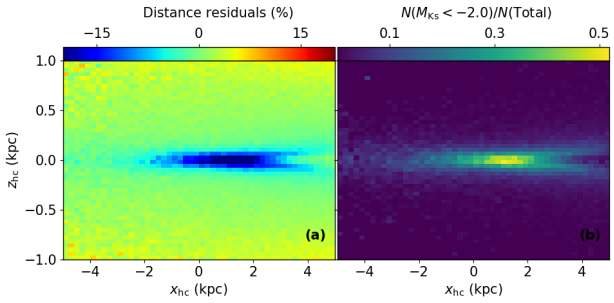

Figure 7. Properties of red-clump stars for a $H < 13.8$ sample simulated with Galaxia. Panel (a) shows the map of distance residuals $(d_{\rm RC} - d_{\rm True})/d_{\rm True}$. It can be seen that close to the plane and towards the Galactic Center, the distance is underestimated. Panel (b) shows the fraction of red-clump stars that are unusually luminous, identified using $M_{\rm Ks} < -2.0$. This suggests that distance errors are due to luminous red-clump stars.

contamination from high-mass RC stars does not extend far away from the mid-plane.

4.2. *Velocity fluctuations in the mid-plane for observed data*

We now discuss the results of our kinematic modeling on the observed datasets and will compare this with selection function matched mock data generated with *Galaxia* as described in Section 3.1. Using red-clump stars from *APOGEE* -DR12, B15 showed that after subtracting an axisymmetric model there remains a high residual in the $V_{\rm los}$ field in the mid-plane ($|z| < 0.25$ kpc). Their kinematical model assumed a flat rotation curve with $V_{\rm circ} = 220$ km s^{-1} and $V_\odot = 22.5$ km s^{-1} and the asymmetric drift was based on the Dehnen distribution (Dehnen 1999). In Figure 8 we consider again the B15 result and explore effects that can lead to enhanced residuals. In Figure 8(a,b) we have reproduced their result by using the same model and data (*APOGEE* -DR12 RC sample) as them. A sharp peak of ≈ 11 km s^{-1} is obtained at a physical scale of about 2.5 kpc similar to B15. The median power spectrum expected due to Poisson noise is shown in dotted black and 68 percentile spread around it based on 20 random realisations is shown in pink.

The location and the height of the peak is essentially unchanged when we include *APOGEE* -DR14 RC sample, the peak only becomes sharper (Figure 8 c,d). Now, B15 used median statistics to compute the residual maps and power spectra. If the distribution of the residual velocity is a Gaussian then employing either mean or median statistics should not make much of a difference in the residual maps. However, if the distribution is asymmetric then it will. In the context of the Galaxy, we know that the V_ϕ distribution is asymmetric (Sharma et al. 2014). Typically one defines a kinematic model and then computes the model parameters that maximize the likelihood of the model given the data. For such a best fit model, it is not clear as to which statistics (mean or median) will give lower values in velocity residual maps. In Figure 8(e,f) we find that choosing mean statistics lowers the power by 0.8 km s^{-1} for the B15 model. We have checked and found that for our best fit *globalRz* model the results remain unchanged for either choice of statistic. So from now on for the rest of our analysis we adopt to use the mean statistics for computing the velocity residual maps.

Next, we consider the volume completeness of the data sample. Figure 9 shows the magnitude distribution of the *GALAH* and *APOGEE* red-clump stars (*GADR14RC* dataset) in V and H passbands. In the mid-plane region most of the data is from *APOGEE* and there is a sharp fall around $H = 12$. Similarly, *GALAH* contributes significantly to the off-plane slices and the distribution falls off around $V = 14$, reflecting the survey selection function. This fall-off limit ($m_{\lambda,\rm max}$) is the faintest magnitude to which stars are observed completely (strictly speaking we mean pseudo-random-complete or unbiased in distance selection) and so we can also estimate the maximum distance this would correspond to by modifying equation 1 as,

$$d_{\rm mod,max} \leq m_{\lambda,\rm max} - M_\lambda - \sigma_{M_\lambda} - A_\lambda. \qquad (15)$$

Using magnitude limits for each slice, extinction factor A_λ , absolute magnitude M_λ and its dispersion σ_{M_λ} from Table 4, we find $d_{\rm max} = 4$ kpc for the mid-plane and $d_{\rm max} = 3.25$ kpc for

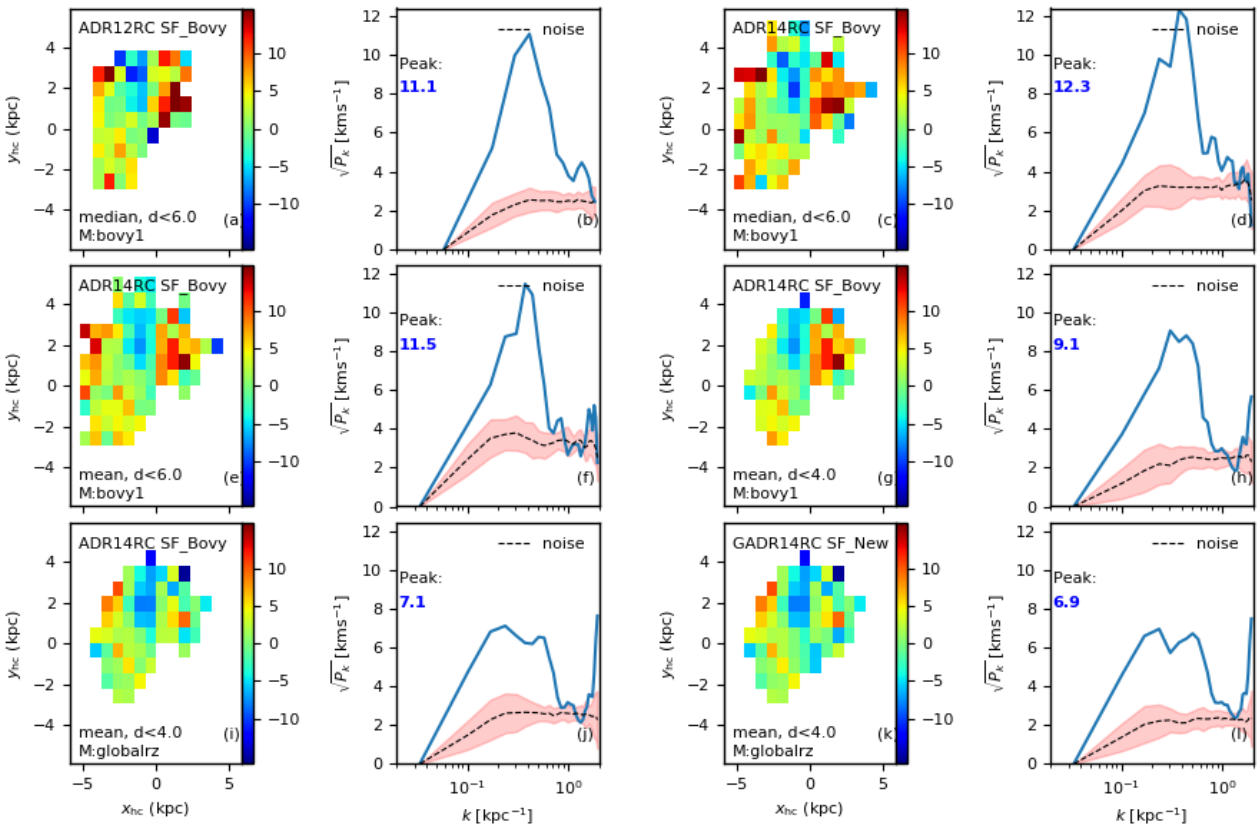

Figure 8. Residual velocity maps and power spectrum for the observed data in the $|z| < 0.25$ kpc slice. Shown are cases for different data sets, with different radial cuts and kinematic models to illustrate the effect of systematics. (a-b) Data used is *APOGEE*_RC_DR12 with stars restricted to radial distance $d < 6$ kpc, using median statistics to compute the residual and using Bovy's analytical model for the kinematics. (c-d) Same as a-b but with *APOGEE*_RC_DR14. (e-f) Same as c-d but now residual is computed using mean statistics. (g-h) Same as e-f but data restricted to $d < 4$ kpc to satisfy volume completeness. (i-j) Same as g-h but we now apply the flexible 2d polynomial kinematic model named as *globalRz* to show it reduces power. (k-l) We apply *globalRz* model to the combined *APOGEE*_DR14 and *GALAH* dataset that uses the new red-clump selection criteria and distance estimation scheme described in the paper.

the off-plane regions. These distance limits are also visible in the scatter plots of Figure 3. After applying the $d < 4$ kpc distance cut, we can see in Figure 8(g,h) that the power in the residual map is reduced to 9.1 km s^{-1}.

Finally, we replace the B15 model with our flexible axisymmetric model from Section 3.3 and this has the effect of further reducing the power down to 7 km s^{-1} in Figure 8(i,j). In Figure 8(k,l) we consider the residuals for the combined dataset *GADR14RC* to increase the sample size and get essentially the same power spectrum as in Figure 8(i,j). A characteristic pattern of blue in first quadrant, red in second and yellow in third as seen in previous cases is also visible here. To conclude, we find that in the mid-plane after accounting for various systematics and a more flexible model the power amplitude can be reduced significantly, though interestingly it cannot be reduced to zero or to the level expected purely due to noise (pink region).

4.3. *Off-plane slices and comparison with Galaxia*

We will now also consider the off-plane ($|z| > 0.25$ kpc) slices of data and will also compare directly with mock realizations using *Galaxia*. Once again, we use the *GADR14RC* dataset and the flexible *globalRz* model. In Figure 10, we show the residual velocity maps, power spectra as well as the $\overline{V}_\phi$ profile for each slice. To take the volume completeness of the sample into account, for the mid-plane slice we have restricted the data to $d < 4.0$ kpc and for the off-plane slices to $d < 3.25$ kpc.

As mentioned already in Section 4.2, the peak power in the mid-plane is around 7 km s^{-1} but moving away from the plane, the power drops (blue solid lines) and is only slightly higher than that expected from noise (dashed lines and the pink zone). Interestingly the mock *Galaxia* samples also predict this trend of high power in the mid-plane but power that is lower and only slightly higher than noise elsewhere. Note, the predicted power spectrum has intrinsic stochasticity due to Poisson noise. So we generate 100 random realisations of the *Galaxia* samples and show the predicted 68% confidence

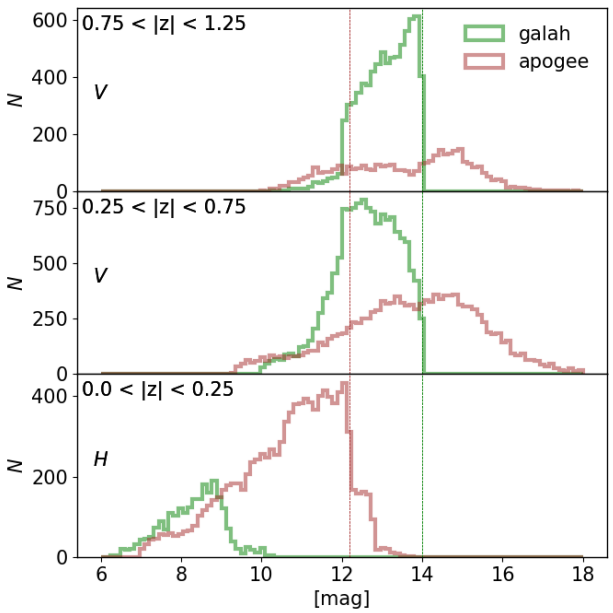

Figure 9. Magnitude distribution for *GALAH* and *APOGEE* red-clump datasets shown for different slices in z (kpc). The position where the magnitude distribution falls sharply sets the maximum distance upto which the stars are unbiased in distance (pseudo volume complete). The magnitude limits are shown by dotted vertical lines. For the off-plane slices the completeness limit is $V = 14$ and set by the *GALAH* survey that dominates the number counts. For the mid-plane slice the limit is $H = 12$ and set by *APOGEE* survey that dominates the number counts.

zone as the green shaded region. From these zones it is clear that for *Galaxia* samples the maximum power achieved in the mid-plane is $4.7^{+1.4}_{-1}$ km s^{-1}. For other slices, for *Galaxia* samples, the green and pink zones are almost on top of each other. However, the maximum power in observed data sets is higher by about 2 km s^{-1} as compared to *Galaxia* samples.

We note that for the observed data and the $0.75 < |z| < 1.25$ slice the $\overline{V}_\phi$ profile obtained using only line-of-sight motion traces well the $\overline{V}_\phi$ profile obtained using both line-of-sight and proper motions. This suggests that for the this slice there is minimal systematic error associated with distance, proper motion or line-of-sight velocities. However, for the other two slices which are closer to the plane we do see differences. The slice closest to the plane shows most pronounced deviations. The mock *Galaxia* samples also show similar behavior. This is most likely due to systematic errors in distances as discussed in Section 4.1. If there are systematic errors with distances then its effect on the inferred $\overline{V}_\phi$ profile will be different depending upon if we infer the profile based on line-of-sight velocities or both line-of-sight velocities and proper motions.

The shape of the rotation profiles for the mock and observed data sets also show differences. For the mock data, the $\overline{V}_\phi$ profile is predominantly flat across all the slices. In contrast, for the observed data a clear variation with R is visible, and the variation becomes more pronounced as we move further away from the mid-plane. While our model is flexible enough to account for simple radial trends in rotation curves, this flexibility can over fit the data if the spatial coverage is not uniform. This is particularly a concern in the mid-plane where the coverage in the (x, y) plane is not uniform, as there is a dearth of stars in the fourth quadrant. This is because both APOGEEE and GALAH have not observed enough stars in the midplane and in the Southern Sky. Basically the constraints on $\overline{V}_\phi$ for $R < 8$ kpc come from data in the first and the fourth quadrant. As evidenced by the red and blue patches in Figure 5b, the systematics in distances lead to incorrect values for the mean $V_{\rm los}$ in the first and the fourth quadrant. If data from only one quadrant is available the model can adjust the value of V_ϕ for $R < 8$ kpc to fit the $V_{\rm los}$ in that quadrant perfectly, however this will not match the mean $V_{\rm los}$ in the other quadrant. If the data from the other quadrant was also available the model would not have the freedom to do this, but in the absence of it the model over fits the data.

Galaxia samples are generated from a simulation and we know its kinematics by design, so we can avoid over fitting a model which is similar to the input model. The input model has kinematics as a function of age, but since we do not have ages in the observed data, we approximate the kinematics by *Strom_z* model which is based on the Stromberg equation and described in Section 3.3. In Figure 11, we employ this new fitting model *Strom_z* for *Galaxia* and compare its results with that of *globalRz* model fitted to the observed data. Overall the trends in velocity maps and the power spectrum for the different slices are the same as in Figure 10, i.e., high power in the mid-plane and negligible power away from the plane. The characteristic pattern of red in first quadrant and yellow in third as seen in observed data for the midplane slice is also reproduced in the midplane slice of the simulated data. For the *Galaxia* samples there is a slight increase in the power by about 2 km s^{-1} for the *Strom_z* as compared to *globalRz*. This is not surprising, as the *globalRz* model is more flexible and has more degrees of freedom than the *Strom_z* model. Moreover, in the plane *globalRz* model can overfit the data due to incomplete coverage of the (x,y) plane.

In Section 4.1, we showed that the presence of high mass RC stars can contaminate the kinematics in the mid-plane and can give rise to high $V_{\rm los}$ residuals. Figure 11(c,f) shows that if we remove this population, by restricting stars to $d_{\rm RC}/d_{\rm true} > 0.8$, the excess power disappears. This suggests that the observed excess power is spurious and is due to contamination from high mass stars whose distances are underestimated. For the off-plane slices this additional cut makes

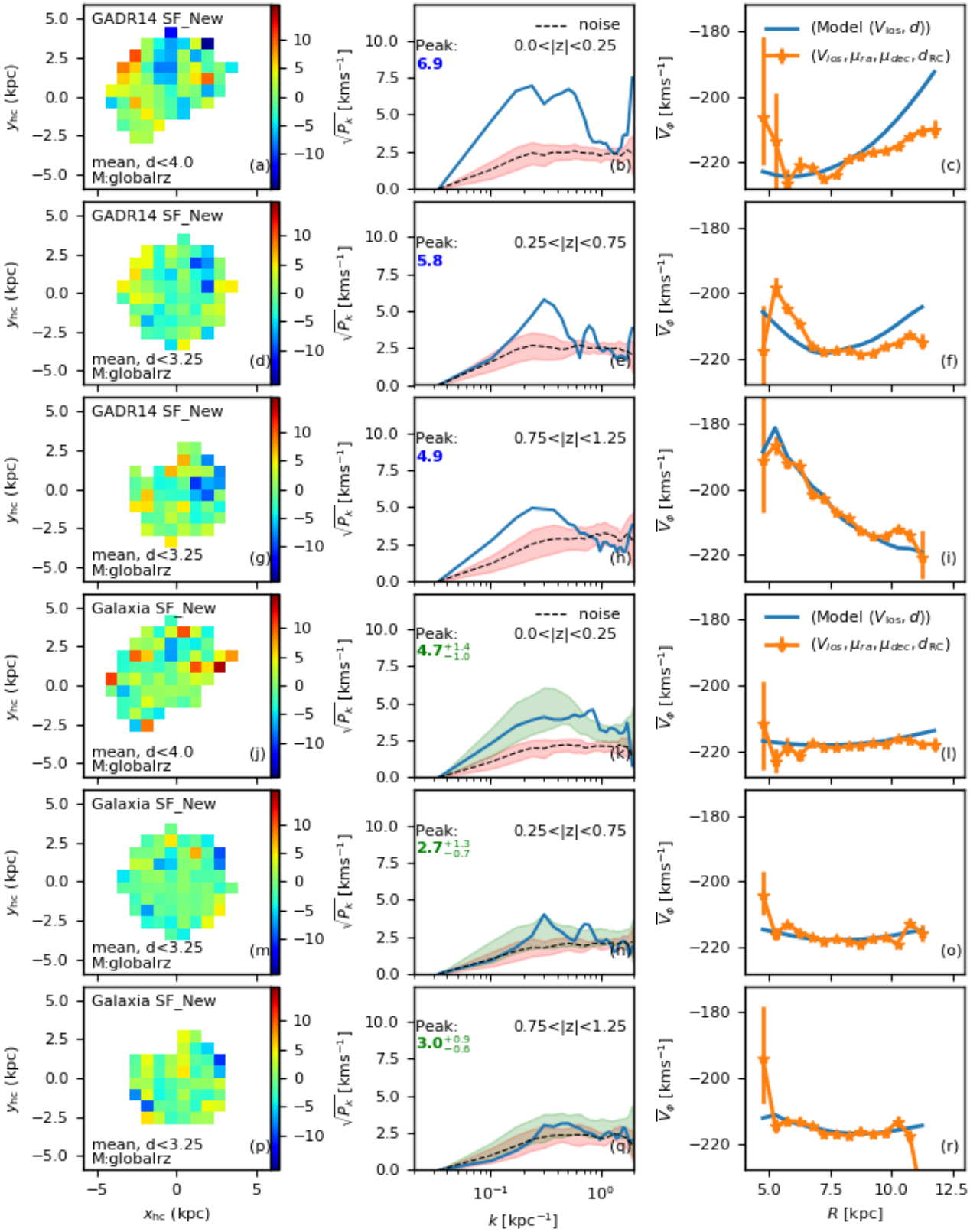

Figure 10. Residual $v_{\rm los}$ velocity maps, power spectrum and $\overline{V}_\phi$ profiles for observed and simulated data for different slices in z. The top three panels correspond to *GADR14RC* while the bottom three panels correspond to mock *Galaxia*. In each case, the power spectrum corresponding to the velocity map is shown in blue, the 1σ noise spread based on 20 random realisations in pink and median noise in dotted black. For *Galaxia* the green region represents the stochastic spread over 100 realisations, in power spectrum with the same selection function as data. We find that except for the case of mid-plane the $\overline{V}_\phi$ profiles are captured well by the *globalRz* models and the power spectrum of residual $v_{\rm los}$ velocity approaches noise with amplitude ≈ 2 km s^{-1}.

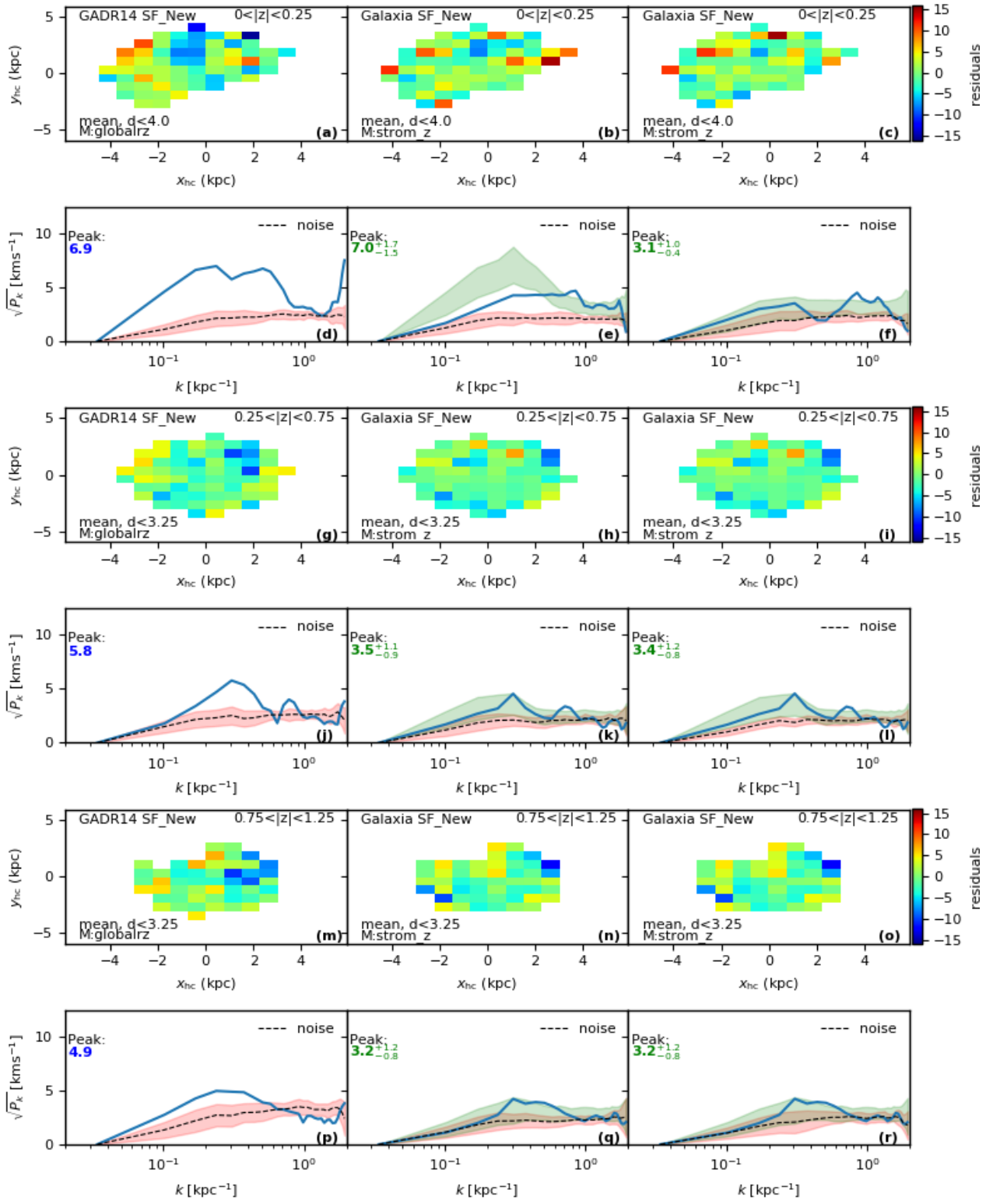

Figure 11. Residual velocity maps and power spectrum for observed and simulated data. Left column shows results of the observed data. Middle column shows results for data simulated with *Galaxia*. Right column also shows results with *Galaxia* but when high mass stars with systematically underestimated distances are removed. First and second rows are for $|z| < 0.25$, third and fourth are for $0.25 < |z| < 0.75$ and fifth and sixth are for $0.75 < |z| < 1.25$. For the observed data a 2d polynomial of degree 3 (nine coefficients) is employed to create the residual velocity map. For simulated data the kinematic model is based on the Stromberg equation and is known a priori.

no difference as the density of high mass RC is negligible for these slices.

5. DISCUSSION AND CONCLUSIONS

Over the past few years several surveys have hinted at non-axisymmetric motion in the disc of the Milky Way. Bovy et al. (2015) used red-clump stars from *APOGEE* to show velocity fluctuations of 11 km s^{-1} in the mid-plane region on scales of 2.5 kpc. In this paper we have made use of all the *APOGEE*-RC stars available up to date along with data from *GALAH*. Our results do not dispute the presence of deviation from mean axis-symmetric motion in the mid-plane of the Galaxy. However, our simulation with *Galaxia* shows that RC samples are likely to be contaminated by intrinsically brighter red-clump stars, which also have higher mass and are younger. Distance is underestimated for such stars. Being young, such stars lie preferentially closer to the mid plane. This has the effect of contaminating the population at any given location with distant stars in that direction whose kinematics is different. This results in strange features when residual velocity maps are constructed in the (x, y) plane.

From Figure 8, we conclude that for the mid-plane slice the peak power $p_{\rm max}$ occurs at physical scales of $k^{-1} \approx 3$ kpc for the observed data, and is either 9.1 km s^{-1}, using the original *Bovy1* model, or 6.9 km s^{-1}, using the more flexible axis-symmetric model *globalRz*. On the other hand, the simulations from *Galaxia* in Figures 10 and 11 show that the peak power is $7.0^{+1.7}_{-1.5}$ km s^{-1}using the *Strom_z* model or $4.7^{+1.4}_{-1}$ km s^{-1}with the flexible *globalRz* model. The peak in the power spectrum is also at the same physical scale of 3 kpc for both the observed sample and *Galaxia* sample. We have also demonstrated that the power in *Galaxia* is due to contamination from young high mass red-clump stars, as the sample with $d_{RC}/d_{\rm True} > 0.8$ does not show excess power. So we do expect the high mass stars to contribute to the power in the observed data, but how much is the contribution from real streaming motion is not obvious at this stage. The streaming and spurious perturbations in the velocity field could be correlated or uncorrelated. For the first case the streaming perturbations will add on to spurious perturbations and will enhance the power linearly. This would mean that the real streaming motion (observed peak power minus the average predicted peak power by *Galaxia*) is less than 2.1 km s^{-1}, adopting either *StromR_z* or *globalRz* as the reference model. If instead they are uncorrelated, we would expect the contributions to be added quadratically (given that power is physically a measure of dispersion), leading to an estimate of 4.8 km s^{-1} using *StromR_z* and 5.1 km s^{-1} using *globalRz*.

In the mid-plane using the flexible *globalRz* model we have been able to reduce the power from 9.1 to 6.9 km s^{-1}. The red pattern in the first quadrant and the yellow in the third are subdued. However, the blue pattern in second quadrant still exists, which could be due to a real feature in the data.

For slices away from the plane, $0.25 < |z| < 0.5$ and $0.5 < |z| < 0.75$, we find that for the observed data the power decreases with height above the plane and is less than 6 km s^{-1}. This rules out large non-axisymmetric streaming motion extending beyond the $|z| > 0.25$ kpc. The *Galaxia* samples also predict very little power (3 km s^{-1}) for slices away from the plane. However, the power in the observed data is higher than that predicted by *Galaxia* by about 2 km s^{-1}. So, small streaming motion is not ruled out.

If the excess power in the observed data is real and not an artefact of high mass clump stars, then it is interesting to consider the cause behind the decrease of power with height. This could be indicative of the fact that it is much easier to excite streaming motion in young dynamically cold populations than old dynamically hot populations.

We note that the analysis presented here has limitations when applied to data away from the mid-plane. The average age of stars increases with height above the plane due to the age scale height relation in the Galaxy. The mean azimuthal motion depends upon age and hence is also a function of $|z|$. Now, if a slice in $|z|$ is not sampled uniformly in the (x, y, z) space, the mean residual motion will show large variance just due to incomplete sampling. It is quite common for spectroscopic surveys to have such incomplete sampling at high $|z|$, as they observe in small patches across the sky. In such cases, one should always compare the power spectrum of observed data with selection function matched mock data which will correctly capture the power due to incomplete sampling.

Lastly, Bovy et al. (2015) using their axis-symmetric model, obtained a power excess in the mid-plane region, of ≈ 12 km $^{-1}$ and strongly suggested that the LSR itself is streaming at this velocity. They add this excess to the Schönrich et al. (2010) value for the Sun's peculiar motion to give the new $V_\odot \approx 12.1 + 12 = 24.1$ km s^{-1}. Following our analysis, we suggest that the adjustment to $V_\odot$ should be no more than 5.1 km s^{-1}, provided the excess power in the residual velocity field is not due to high-mass red-clump stars.

In near future, *GAIA* can resolve some of the questions raised by our analysis. First, with accurate parallaxes from *GAIA*, we can confirm if the *APOGEE* red-clump catalog contains high mass stars with underestimated distances. If so, then does removing this population get rid of the excess power in the residual velocity map? Moreover, with proper motion we can construct and study velocity maps of V_ϕ, V_R and V_z separately instead of just $V_{\rm los}$. We can also make use of all type of stars and not just red-clumps.

Acknowledgements: This research has made use of Astropy13, a community-developed core Python package for

Astronomy (Astropy Collaboration et al., 2013). This research has made use of NumPy (Walt et al., 2011), SciPy, and MatPlotLib (Hunter, 2007).

REFERENCES

Altmann, M., Roeser, S., Demleitner, M., Bastian, U., & Schilbach, E. 2017, A&A, 600, L4

Anguiano, B., Rebassa-Mansergas, A., García-Berro, E., et al. 2017, MNRAS, 469, 2102

Antoja, T., de Bruijne, J., Figueras, F., et al. 2017, A&A, 602, L13

Bertelli, G., Bressan, A., Chiosi, C., Fagotto, F., & Nasi, E. 1994, A&AS, 106, 275

Binney, J., & Tremaine, S. 2008, Galactic Dynamics: Second Edition (Princeton University Press)

Binney, J., Burnett, B., Kordopatis, G., et al. 2014, MNRAS, 437, 351

Bland-Hawthorn, J., & Gerhard, O. 2016, ARA&A, 54, 529

Bovy, J. 2010, ApJ, 725, 1676

Bovy, J., Bird, J. C., García Pérez, A. E., et al. 2015, ApJ, 800, 83

Bovy, J., Allende Prieto, C., Beers, T. C., et al. 2012, ApJ, 759, 131

Bovy, J., Nidever, D. L., Rix, H.-W., et al. 2014, ApJ, 790, 127

Bressan, A., Marigo, P., Girardi, L., et al. 2012, MNRAS, 427, 127

Cannon, R. D. 1970, MNRAS, 150, 111

Casagrande, L., Ramírez, I., Meléndez, J., Bessell, M., & Asplund, M. 2010, A&A, 512, A54

Chen, Y., Bressan, A., Girardi, L., et al. 2015, MNRAS, 452, 1068

Chen, Y., Girardi, L., Bressan, A., et al. 2014, MNRAS, 444, 2525

Dehnen, W. 1998, AJ, 115, 2384

—. 1999, AJ, 118, 1201

Duong, L., Freeman, K. C., Asplund, M., et al. 2018, ArXiv e-prints, arXiv:1801.01514

Gaia Collaboration, Brown, A. G. A., Vallenari, A., et al. 2016, A&A, 595, A2

Girardi, L. 2016, ARA&A, 54, 95

Hawkins, K., Leistedt, B., Bovy, J., & Hogg, D. W. 2017, ArXiv e-prints, arXiv:1705.08988

Holtzman, J. A., Shetrone, M., Johnson, J. A., et al. 2015, AJ, 150, 148

Hunt, J. A. S., Bovy, J., Pérez-Villegas, A., et al. 2018, MNRAS, 474, 95

Kos, J., Lin, J., Zwitter, T., et al. 2017, MNRAS, 464, 1259

Kunder, A., Kordopatis, G., Steinmetz, M., et al. 2017, AJ, 153, 75

Majewski, S. R., Skrutskie, M. F., Weinberg, M. D., & Ostheimer, J. C. 2003, ApJ, 599, 1082

Majewski, S. R., Zasowski, G., & Nidever, D. L. 2011, ApJ, 739, 25

Marigo, P., Girardi, L., Bressan, A., et al. 2008, A&A, 482, 883

Martell, S. L., Sharma, S., Buder, S., et al. 2017, MNRAS, 465, 3203

Miglio, A., Chiappini, C., Mosser, B., et al. 2017, Astronomische Nachrichten, 338, 644

Nordström, B., Mayor, M., Andersen, J., et al. 2004, A&A, 418, 989

Reid, M. J., & Brunthaler, A. 2004, ApJ, 616, 872

Robin, A. C., Bienaymé, O., Fernández-Trincado, J. G., & Reylé, C. 2017, ArXiv e-prints, arXiv:1704.06274

Robin, A. C., Reylé, C., Derrière, S., & Picaud, S. 2003, A&A, 409, 523

Roeser, S., Demleitner, M., & Schilbach, E. 2010, AJ, 139, 2440

Salaris, M., & Girardi, L. 2002, MNRAS, 337, 332

Schlegel, D. J., Finkbeiner, D. P., & Davis, M. 1998, ApJ, 500, 525

Schönrich, R., Binney, J., & Dehnen, W. 2010, MNRAS, 403, 1829

Sharma, S. 2017, ArXiv e-prints, arXiv:1706.01629

Sharma, S., & Bland-Hawthorn, J. 2013, ApJ, 773, 183

Sharma, S., Bland-Hawthorn, J., Johnston, K. V., & Binney, J. 2011, ApJ, 730, 3

Sharma, S., Stello, D., & Bland-Hawthorn, J. 2016, Astronomische Nachrichten, 337, 875

Sharma, S., Bland-Hawthorn, J., Binney, J., et al. 2014, ApJ, 793, 51

Sharma, S., Stello, D., Buder, S., et al. 2018, MNRAS, 473, 2004

Stewart, K. R., Bullock, J. S., Wechsler, R. H., Maller, A. H., & Zentner, A. R. 2008, ApJ, 683, 597

Tang, J., Bressan, A., Rosenfield, P., et al. 2014, MNRAS, 445, 4287

Wegg, C., Gerhard, O., & Portail, M. 2015, MNRAS, 450, 4050

Williams, M. E. K., Steinmetz, M., Binney, J., et al. 2013, MNRAS, 436, 101

Wittenmyer, R. A., Sharma, S., Stello, D., et al. 2018, AJ, 155, 84

Zacharias, N., Finch, C., & Frouard, J. 2017, AJ, 153, 166

Zacharias, N., Finch, C. T., Girard, T. M., et al. 2013, AJ, 145, 44

Zasowski, G., Johnson, J. A., Frinchaboy, P. M., et al. 2013, AJ, 146, 81

Zhao, G., Zhao, Y., Chu, Y., Jing, Y., & Deng, L. 2012, ArXiv e-prints, arXiv:1206.3569

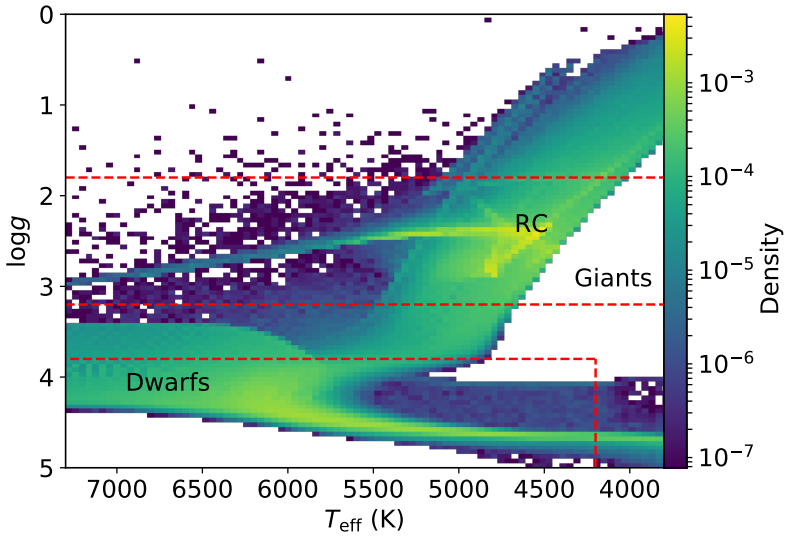

Figure 12. Spectroscopic HR diagram of the *Galaxia* $J < 15$ all-sky sample used to derive $(J-K)_0$ as a function of $T_{\rm eff}$ and $\log g$. Red dashed lines mark the approximate boundary between Dwarfs and Giants and the typical location of red-clump (RC) is indicated.

APPENDIX

A. RED-CLUMP CALIBRATION AND SELECTION

Following from Section 2.1, here we describe details of our red-clump selection and calibration. A crude sample of RC stars can be selected based on cuts in surface gravity $\log g$ and dereddened color $(J-K)_0$, for example, Williams et al. (2013) used the simple cuts of $1.8 \leq \log g \leq 3.0$ and $0.55 < (J-K)_0 < 0.8$ on *RAVE* data. However, this was estimated to be contaminated by about 30-60 % of non-RC stars (including secondary red-clump and the RGB bump). In the APOGEE-RC catalog Bovy et al. (2014) use PARSEC isochrones (Bressan et al. 2012) and asteroseismic constraints to improve the sample purity, resulting in the following comprehensive selection scheme

$$1.8 \leq \log g \leq 0.0018 \left(T_{\rm eff} - T_{\rm eff}^{\rm ref}([{\rm Fe/H}])\right) + 2.5\,, \tag{A1}$$

$$Z > 1.21[(J-K)_0 - 0.05]^9 + 0.0011, \tag{A2}$$

$$Z < {\rm Min}\left(2.58[(J-K)_0 - 0.40]^3 + 0.0034, 0.06\right), \tag{A3}$$

$$0.5 < (J-K)_0 < 0.8, \tag{A4}$$

where,

$$T_{\rm eff}^{\rm ref}([{\rm Fe/H}]) = -382.5[{\rm Fe/H}] + 4607\,{\rm K}\,. \tag{A5}$$

However, this requires de-reddened $(J-K)_0$ color and to get them extinction is required. In the *APOGEE* red-clump catalog by Bovy et al. (2014) extinction was estimated using the Rayleigh Jeans Color Excess method (RJCE; Majewski et al. (2011)) which requires photometry in $[4.5\mu]$ band. Extinction estimates based purely on photometry are useful but have inaccuracies associated with them. To overcome this, we use pure red-clumps from *Galaxia* to derive empirical relations expressing $(J-K)_0$ in terms of spectroscopic parameters [Fe/H] and $T_{\rm eff}$. Such relations have previously been derived for K-type dwarf stars by Casagrande et al. (2010), where one fits for a function of the form

$$5040/T_{\rm eff} = a_0 + a_1 X + a_2 X^2 + a_3 XY + a_4 Y + a_5 Y^2, \tag{A6}$$

where X = $(J-K)_0$, Y = [Fe/H] and $(a_0 ... a_5)$ are the fit coefficients. While this is a valid function to use, it is not analytically invertible to derive $(J-K)_0$, unless the dependence on [Fe/H] can be neglected in which case equation A6 can be easily inverted

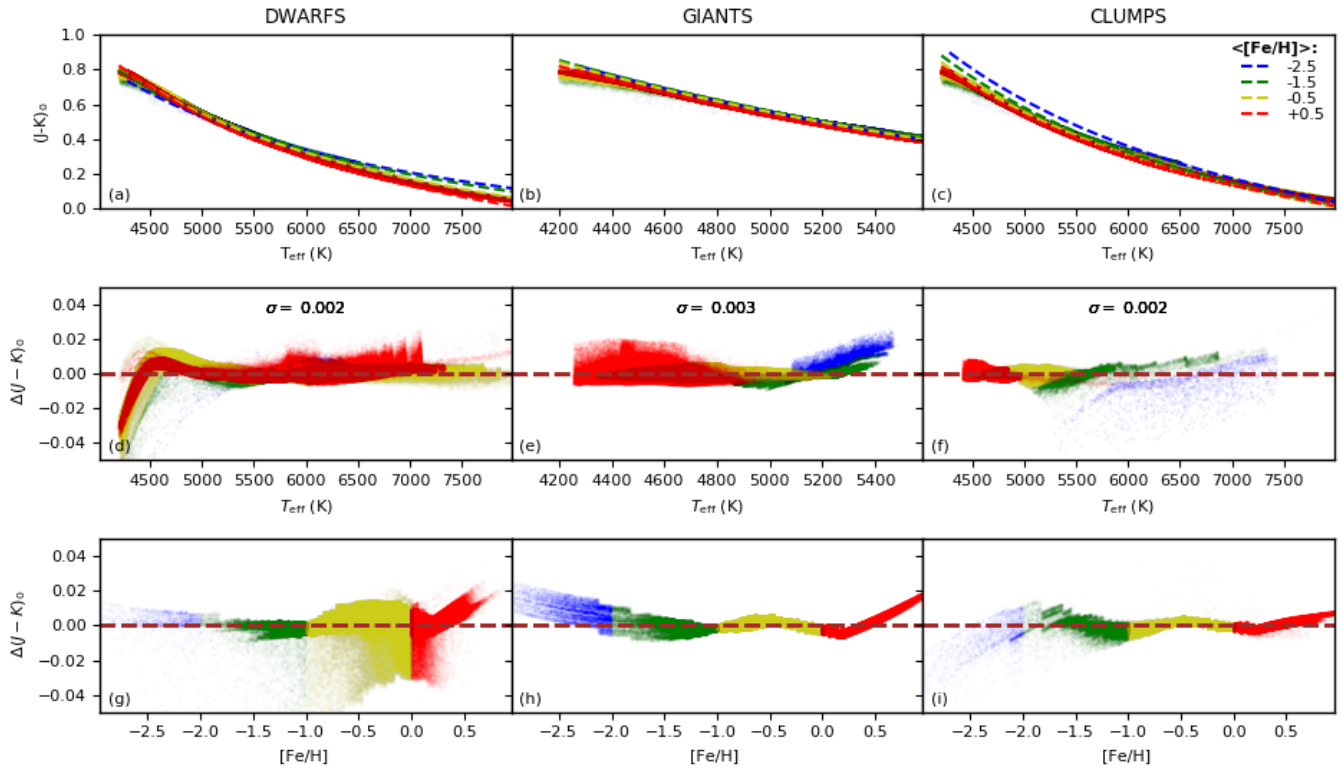

Figure 13. Empirical ($(J-K)_0$ |$T_{\rm eff}$, $\log g$) calibration using *Galaxia* all-sky sample based on equation A8: Panels (a,b,c) show the best-fit (dotted curves) for Dwarfs, Giants and Red-clump stars and the color-coding is the mean [Fe/H]. Panels (d,e,f) and (g,h,i)show the residuals against temperature $T_{\rm eff}$ and [Fe/H] respectively. While for Dwarfs the derived relations fit well at low metallicity and high temperatures, for the Giants and Red-clump, residuals are low everywhere except for at [Fe/H]<-2.

to give[7]

$$(J-K)_0 \sim \frac{1}{2a_2}[-a1+\sqrt{a_1^2-4a_2(a_0-\frac{5040}{T_{\rm eff}})}]. \tag{A7}$$

We show below that the dependence on [Fe/H] is weak but not negligible. So we alter equation A6 to fit directly for $(J-K)_0$ as

$$(J-K)_0 = a_0+a_1X+a_2X^2+a_3XY+a_4Y+a_5Y^2, \tag{A8}$$

where X =[Fe/H] and $Y = 5040/T_{\rm eff}$.

To derive the coefficients, we use data simulated by the code *Galaxia*, which allows us to obtain relations valid for majority of the stars that we observe. More specifically, we generate an all-sky catalogue with $J < 15$, where the stellar parameters are generated using PARSEC[8] isochrones (Bressan et al. (2012); Chen et al. (2014); Chen et al. (2015); Tang et al. (2014)) and choose the 2MASSWISE photometric system. From this we select three populations using boundaries in $\log g$, namely Dwarfs ($\log g \geq 3.8$), Giants ($\log g \geq 3.2$), and red-clump stars ($1.8 \leq \log g \leq 3.0$). Figure 12 marks the approximate boundaries between the three populations in the spectroscopic HR diagram. For a given age and metallicity of a star, stellar models can predict the initial mass required to reach the tip of the giant branch, and so for red-clump stars the initial mass must exceed this threshold tipping mass (i.e $> M_{\rm RGB,tip}$). We make this additional cut to identify the real red-clump stars in *Galaxia*. We also exclude M-dwarfs from our analysis by applying a temperature cut of $4200 < T_{\rm eff}(K) < 8000$, as the $(J-K)$ color is not a good indicator of temperature for them.

The resulting best-fit coefficients ($a_0 ... a_5$) for each population are listed in Table 3, using which we derive $(J-K)_0$. Figure 13 shows the predicted $(J-K)_0$ and residuals as a function of $T_{\rm eff}$ and [Fe/H]. The best-fit curves trace the color well and the residuals

[7] For completion we also perform the fitting using equation A6 with and without the [Fe/H] term and found that the derived temperature had residuals below 20 K for Clumps and Giants though Dwarfs had higher (≈50 K) residuals without the [Fe/H] term. We provide these results in Table 6 but do not use it for our analysis in this paper.

[8] The iscochrones were downloaded from http://stev.oapd.inaf.it/cmd

Table 3. Best-fit coefficients for equation A8 used to derive $(J-K)_0$ for the three populations: Dwarfs, Giants and Red-clump. The fitting is carried out over the temperature range $4200<T_{\rm eff}<8000$.

Population	a_0	a_1	a_2	a_3	a_4	a_5
Dwarfs	-0.637	-0.107	-0.007	0.093	0.915	0.251
Giants	-0.957	0.000	-0.006	-0.020	1.489	0.002
Red-clump	-0.800	0.046	0.008	-0.060	1.199	0.132

Table 4. Median absolute magnitude $M_{\rm RC}$, and dispersion in absolute magnitude $\sigma_{M_{\rm RC}}$ for red-clump stars selected from *Galaxia* using the scheme in Appendix A. We have tabulated the values for a few common passbands only for a comparison with literature. Also listed are the extinction factors (f_λ) for the four passbands and these are taken from Schlegel et al. (1998).

Passband (λ)	$M_{\rm RC}$	$\sigma_{M_{\rm RC}}$	$f_\lambda = \frac{A_\lambda}{E(B-V)}$
J	−0.98	0.11	0.902
H	−1.52	0.12	0.576
K	−1.60	0.13	0.367
V_{JK}	+0.75	0.15	3.240

Table 5. Tabulated values for mean absolute magnitude $M_{\rm Ks}$ as function of [Fe/H] as derived with *Galaxia* (red line inFigure 15a). Distances to red-clump stars are estimated by linear interpolating over these values.

[Fe/H] (dex)	-0.8	-0.7	-0.6	-0.5	-0.4	-0.3	-0.2	-0.1	0.0	0.1	0.2	0.3	0.4
$M_{\rm Ks}$	-1.390	-1.405	-1.442	-1.475	-1.520	-1.564	-1.598	-1.622	-1.633	-1.646	-1.659	-1.666	-1.676

for all three populations are below 0.003 mag. As mentioned earlier, weak metallicity dependence is visible. For the red-clump and giants, the residuals show very little variation with temperature (Figure 13e and f), but with metallicity (Figure 13h and i) a systematic effect can be seen for [Fe/H]< -2. In comparison for dwarfs higher metallicities and lower temperatures have high residuals (Figure 13d and g).

Finally using these derived colors we can now use equations A1-A4 to produce a sample of red-clump stars from our mock $J < 15$ *Galaxia* catalogue. Here and throughout the paper for the purpose of selection function we make use of the $(J-K)_0$ relation corresponding to the red-clump stars. Figure Figure 14 shows the red-clump selection in metallicity-color space and illustrates the effect of applying additional cuts from equations A2 and A3 (using color-temperature-metallicity selection) in order to remove contamination from non-RC stars. It is clear that the final selection has a very narrow range in the median $M_{\rm k}$ and lies around -1.60.

With the RC sample selected, in Figure 15 we plot the $M_{\rm K}$ against [Fe/H] and a running median curve (shown in red) that can be used to approximate red-clump magnitude from metallicity. The dispersion in estimated distance modulus ($\sigma_{\rm dmod}$) increases from 0.1 to 0.16 by adding spectroscopic errors, however, if the uncertainty in temperature is a factor of two lower this lower $\sigma_{\rm dmod}$ to 0.12. For the GALAH data we can get such precision for good signal to noise data (Duong et al. 2018; Sharma et al. 2018).

For some simple calculations it is useful to know the typical absolute magnitude of red-clump stars in different photometric bands, e.g., to estimate the volume completeness of various surveys. Hence, in Table 4 we list the median absolute magnitude and dispersion based on 68% confidence region for the J, H, K and V_{JK} pass bands. Here,

$$V_{JK} = Ks + 2.0(J-Ks+0.14) + 0.382\exp[(J-Ks-0.2)/0.50] \tag{A9}$$

is the Johnson V band magnitude computed using *2MASS* magnitudes (Sharma et al. 2018). Our derived values are in good agreement with literature (Girardi 2016).

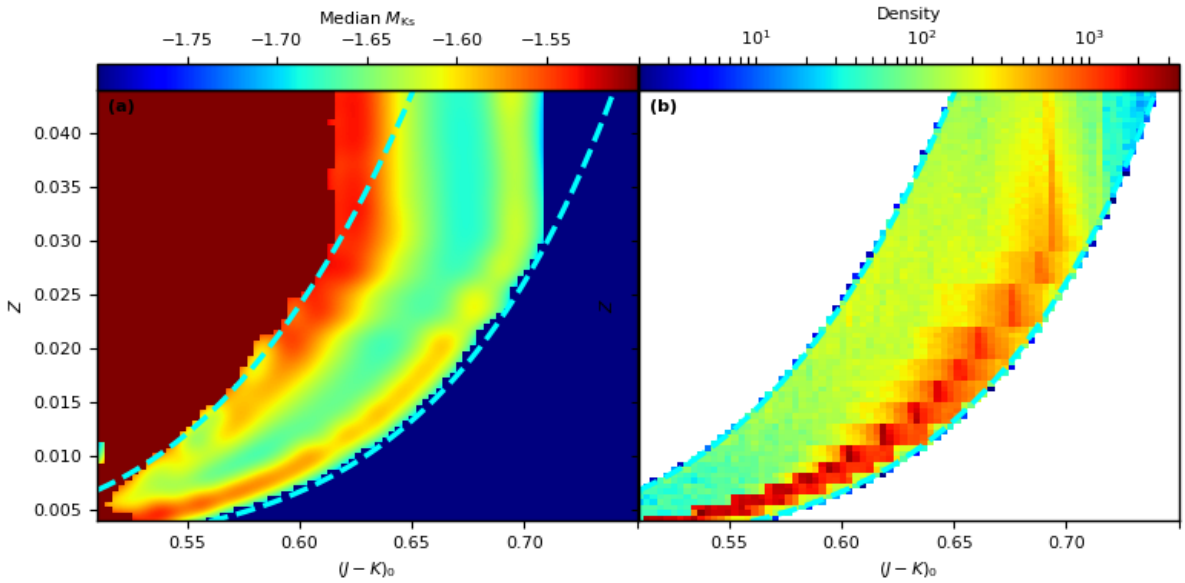

Figure 14. The all-sky *Galaxia* red-clump sample selected using $T_{\rm eff}$ and $\log g$ cuts based on equations A1 and A4, and with additional cuts (cyan dotted line) based on equations A2 and A3 using Color-Temperature-metallicity calibration necessary to remove contamination from non RC stars. In the final selected sample, the median $M_{\rm k}$ lies in a narrow band around -1.60 (Panel a) and most stars are concentrated around this value (Panel b).

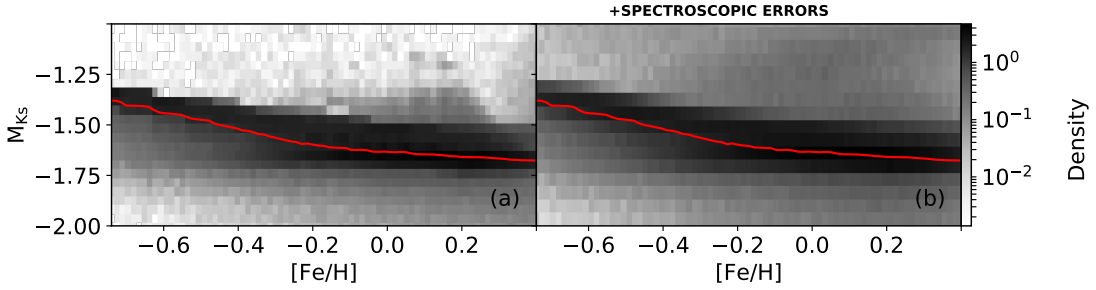

Figure 15. $M_{\rm K}$ - [Fe/H] distribution for the *Galaxia* red-clump sample. (a) This is the case without any errors in spectroscopic parameters. The sample has a tight distribution with dispersion in estimated distance modulus of $\sigma_{\rm dmod} = 0.1$; the running average (solid red curve) can thus be used to derive absolute magnitude $M_{\rm K}$ from spectroscopy. (b) This is the case with spectroscopic errors of $(\sigma_{\log T_{\rm eff}}, \sigma_{\rm [Fe/H]}, \sigma_{\log g}) = (0.011, 0.05, 0.1)$ dex. Here dispersion in distance modulus increases to $\sigma_{M_{\rm k}} = 0.18$. The red curve is same as in (a).

Table 6. Best-fit coefficients for equation A6 for the three populations: Dwarfs, Giants and Red-clump stars. Equation A6 derives $5040/T_{\rm eff}$ which can be analyticaly be inverted to derive $(J-K)_0$ if we neglect the [Fe/H] term. This alters the coeffecients slightly and so we also list that case. Note: This table is only provided for completion and we do not use it for our analysis in this paper.

Population	[Fe/H] used?	a_0	a_1	a_2	a_3	a_4	a_5	N
dwarfs	yes	0.5985	0.8148	-0.104	-0.053	0.0382	0.0045	212120
dwarfs	no	0.6045	0.7700	-0.051	-	-	-	212120
Red-clump	yes	0.6511	0.6410	0.0298	-7e-05	0.0116	-0.002	141666
Red-clump	no	0.5701	0.8421	-0.083	-	-	-	141666
giants	yes	0.6447	0.6651	0.0010	0.0044	0.0113	0.0042	135891
giants	no	0.5458	0.9260	-0.171	-	-	-	135891

Table 7. Location and amplitude of peaks in residual velocity power spectra for the observed data and the *Galaxia* samples. For *Galaxia* samples 16, 50 and 84 percentile values based on 100 random realisations are given.

Slice (kpc)	Data		*Galaxia*							
			Strom_z				*globalRz*			
	k^{-1} kpc	$P(k)$	k^{-1} kpc	$P(k)_{16}$	$P(k)_{50}$	$P(k)_{84}$	k^{-1} kpc	$P(k)_{16}$	$P(k)_{50}$	$P(k)_{84}$
$0.00 < \|z\| < 0.25$	0.30	6.90	0.30	5.50	7.00	8.70	0.30	3.70	4.70	6.10
$0.25 < \|z\| < 0.75$	0.31	5.80	0.30	2.60	3.50	4.60	0.30	2.00	2.70	4.00
$0.75 < \|z\| < 1.25$	0.26	4.90	0.30	2.40	3.20	4.40	0.40	2.40	3.00	3.90